Intercomparison Project (CMIP6) models and the strength of the cloud feedback (Wang et al. 2021), which is the greatest contributor to the uncertainty in estimates of equilibrium or effective climate sensitivity (ECS) among CMIP6 generation climate models (Zelinka et al. 2020; Bellouin et al. 2020; Gettelman et al. 2019). While the spread in the total aerosol radiative forcing is uncorrelated with the spread in ECS (Huusko et al. 2021; Meehl et al. 2020; Smith et al. 2020), modifications and tuning of AIE can affect the ECS estimate produced by Earth system models (ESMs) (Gettelman et al. 2019).

Given the importance of the AIE and its large contribution to the total anthropogenic radiative forcing and relationship with ECS uncertainties, efforts to constrain the understanding of the AIE are essential. It is well recognized in the literature that AIE is dependent on background aerosol loading (Twomey 1977; Boucher et al. 2013; Carslaw et al. 2013; Wilcox et al. 2015; Grandey and Wang 2019), but there has been no assessment to date of the potential dependence of AIE on total background climate conditions, such as combined changes to cloud properties and atmospheric humidity. Studies suggest that the cloud radiative effect response to aerosol–cloud interactions depends on the local meteorologic variability in the shallow boundary layer cumuli over land (Glenn et al. 2020) and warm marine cloud regimes (Douglas and L'Ecuyer 2019). However, the explicit dependence of AIE strength on the background climate state, given the combined changes in cloud fields and other meteorological conditions expected with warming, has not been addressed in other studies. Investigation of the AIE dependence on background climate is vital because the climate system and atmospheric environment have and will continue to evolve, predominantly due to greenhouse gas warming, which leads us to speculate that the AIE has also evolved with this changing climate (Boucher et al. 2013; Myhre et al. 2013; Forster et al. 2021). Furthermore, understanding the potential dependence of the AIE and aerosol radiative forcing on background climate is essential for simulation design, since evolving or constant forcings determine the background climate state.

AIE manifests where anthropogenic aerosols interact with susceptible cloud regimes. Collocation of spatially heterogeneous anthropogenic aerosol with geographically diverse cloud types is thus an important determinant of the overall AIE strength (Douglas and L'Ecuyer 2019). There are several warming-driven changes in cloud fields and background meteorological conditions that could be expected to impact the strength of the AIE and aerosol effective radiative forcing, which we outline and present initial hypotheses for below. Current models show that anthropogenic warming throughout the historical period has led to many cloud changes, denoted as the cloud feedback, which is positive across almost all CMIP6 models (Sherwood et al. 2020; Zelinka et al. 2020, 2017; Forster et al. 2021). The total positive cloud feedback is commonly separated into individual feedbacks of specific cloud regimes or cloud components in order to identify the strongest contributors to the total cloud feedback. The dominant individual cloud feedbacks include the positive tropical and subtropical marine low cloud feedback, positive high cloud altitude feedback, and negative extratropical cloud optical depth feedback, dominated by the positive low cloud feedbacks (Sherwood et al. 2020; Zelinka et al. 2020; Forster et al. 2021). Additionally, the water vapor feedback and surface albedo feedback (Forster et al. 2021) could affect AIE strength through their modification of the radiative properties of the Earth system.

Expected positive tropical and subtropical marine low cloud feedbacks in response to warming (Forster et al. 2021; Sherwood et al. 2020) could be expected to decrease both AIE and ADE. Sea surface temperature (SST) warming weakens the boundary layer temperature inversion and dehydrates the low cloud layer within the marine stratocumulus decks via convective mixing and increased cloud-top entrainment, breaking up the consistent stratocumulus and trade cumulus cloud regimes on the eastern side of ocean basins, thereby decreasing shortwave reflectivity (Forster et al. 2021; Sherwood et al. 2020; Boucher et al. 2013; Qu et al. 2014; Sherwood et al. 2014). This has recently been shown to be sensitive to the spatial pattern of SST warming, denoted as the "pattern effect" (Rugenstein et al. 2023; Wills et al. 2022; Seager et al. 2022; Dong et al. 2019; Ceppi and Gregory 2017; Zhou et al. 2017). The collocation of the continental outflow of California coastal (Hegg et al. 2010), trans-Pacific Asian (Heald et al. 2006; Hoell et al. 1997), and southeast Pacific Andes (Mechoso et al. 2014) anthropogenic aerosols with this expected decrease in persistent eastern Pacific marine stratocumulus clouds with warming could lead to decreased global-mean AIE in the warmed climate state, since these regimes are responsible for a significant amount of the AIE globally. Furthermore, a less humid lower troposphere in certain regions between background climates could lead to less hygroscopic growth of aerosols, which would decrease the ADE once aerosols are imposed in that changed background climate state.

The positive high cloud altitude feedback in response to warming may be expected to have little impact on AIE and ADE, at least as presently represented in most Earth system models. According to the fixed anvil temperature (FAT) hypothesis, the temperature of the convective detrainment layer will not change with atmospheric warming. Consequently, cloud-top altitude changes but not longwave emission (Hartmann and Larson 2002). Thus, the increased surface warming leads to more longwave radiation being trapped below the clouds and a high cloud greenhouse effect (Forster et al. 2021; Zelinka and Hartmann 2010; Hartmann and Larson 2002). Aerosols initiate the formation of ice nuclei (IN) in mixed phase and ice clouds, so anthropogenic aerosol perturbations have the potential to affect glaciation rate, ice optical properties, cloud amount, and hence, high cloud radiative effects (Boucher et al. 2013; Storelvmo 2017; Forster et al. 2021). However, some relationships between aerosols and IN are unclear due to complicated nonlinearities and variations in surrounding environmental conditions and are generally not well represented in CMIP6 models (Boucher et al. 2013; Forster et al. 2021). Hence, the total contribution of the high cloud altitude feedback on AIE and ADE in most Earth system models could be weak, given the uncertainties associated with high cloud AIE.

The effect of the expected extratropical cloud optical depth feedback with atmospheric warming on AIE and ADE is difficult to determine due to limited observations and process representation but is expected to be weak. The immediate phase change from cloud ice to liquid droplets with warming in the midlatitudes is theorized to increase cloud shortwave reflectivity (Bjordal et al. 2020; Tan et al. 2016; Forster et al. 2021). However, the comparison of AIE and ADE in cold clouds versus warm clouds is complicated due to the lack of observations for aerosol interactions in cold clouds (Patnaude and Diao 2020; Forster et al. 2021). The extratropical cloud optical depth feedback has been shown to be small and heavily outweighed by the positive feedbacks from decreasing low clouds and rising high cloud tops, so these effects on AIE and ADE are expected to be negligible (Bjordal et al. 2020; Forster et al. 2021; Sherwood et al. 2020). Furthermore, this extratropical phase-change feedback is weak in most CMIP6 models (Bjordal et al. 2020; Sherwood et al. 2020; Tan et al. 2016; Forster et al. 2021).

The water vapor and ice albedo feedbacks can both be expected to strengthen ADE. With atmospheric warming, the Clausius–Clapeyron equation suggests that the atmospheric water vapor content will increase, particularly in the upper troposphere (Boucher et al. 2013; Forster et al. 2021), thereby further increasing atmospheric water vapor due to the enhanced greenhouse effect (Boucher et al. 2013; Forster et al. 2021). A more humid atmosphere would be expected to increase hygroscopic growth and the ADE. Reduced surface albedo due to sea ice amount and extent reductions with surface warming, meanwhile, would decrease the total reflectivity in the affected area. However, the reflectivity of added anthropogenic aerosols above the newly darkened surface below would be expected to manifest as stronger ADE, despite the total planetary albedo decreasing.

Based on the first principles of how atmospheric conditions should change with global warming, we hypothesize that the strength of the AIE should be dependent on the background climate state. We further hypothesize that the expected decrease of eastern Pacific tropical and subtropical marine low clouds with global warming will strongly contribute to a decrease in AIE with warming, given the importance of these regimes for global-mean AIE. Although global low cloud feedback radiative strength estimates in response to present-day warming are on the order of 1%–2% of total shortwave cloud forcing (e.g., Myers et al. 2021; Sherwood et al. 2020), the spatial heterogeneity of these changes relative to the geographic location of increased anthropogenic aerosol loading (Carslaw and Pringle 2022; Hegg et al. 2010; Heald et al. 2006; Hoell et al. 1997), the known nonlinearities in aerosol–cloud interactions (Twomey 1977; Boucher et al. 2013; Carslaw et al. 2013), and the potential contribution from aerosol interaction with other cloud types leaves the potential for dependence of AIE strength on these shifts in background cloud and atmospheric and surface conditions as a critical open question. Proving or disproving this hypothesis could contribute to the understanding of how AIE is expected to behave in a future climate state with global warming, which could help constrain the behavior of the total anthropogenic aerosol forcing and ECS estimates. The validity of this hypothesis is also important for interpretation of the AIE quantified from ESM simulations that use different experiment designs, since this alters the background climate from which the AIE is calculated. In this study, we explicitly test these hypotheses via a novel suite of simulations in the National Center for Atmospheric Research (NCAR) Community Earth System Model 2, version 2.1.3 (CESM2), that isolates the effect of background climate state on the aerosol effective radiative forcing strength. The following sections discuss the simulation design used to explore this topic (section 2), the resulting AIE, ADE, cloud, and atmospheric changes seen between the preindustrial, present-day, and idealized extremely warm climates (section 3), and implications of the results for our understanding of the behavior of aerosol forcing in a changing climate (section 4).

2. Methodology

a. *Prescribed SST simulations in NCAR CESM2*

This study uses prescribed SST simulations, conducted in CESM2, developed by NCAR, and included in CMIP6. This CESM2 configuration includes the Community Atmosphere Model, version 6.0 (CAM6), with a horizontal grid spacing of 1.25° longitude by 0.9° latitude, 32 vertical layers, model top height at approximately 40 km, or 2.26 hPa, and limited stratospheric chemistry (Danabasoglu et al. 2020). CAM6 includes the Cloud Layers Unified by Binormals (CLUBB) that unifies the shallow-convection, boundary layer, and larger-scale condensation schemes previously present in CAM5 (Danabasoglu et al. 2020). CAM6 includes an updated two-moment bulk stratiform cloud microphysics scheme with prognostic precipitation, the Morrison–Gettelman cloud microphysics scheme (MG2), and parameterizations that allow for mixed-phase and ice nucleation on aerosols in addition to the formation via temperature (Gettelman and Morrison 2015; Hoose et al. 2010; Wang et al. 2014; Shi et al. 2015). CAM6 is coupled to the Community Land Model, version 5 (CLM5; Lawrence et al. 2019). The imposed SSTs for this study (Fig. 12 in the online supplemental material) are obtained from the merged Hadley–NOAA/OI sea surface temperature and sea ice concentration (SIC) datasets (Hurrell et al. 2008) taken from the Met Office Marine Data Bank (MDB). This SST and SIC dataset is specifically designed for AMIP-style simulations using the Community Atmosphere Model but may differ slightly from the current generation AMIP dataset (Taylor et al. 2000). The Hadley Centre Sea Ice and Sea Surface Temperature dataset, version 1.1 (HadISST), taken from the MDB with bias-adjusted in situ observations from 1870 to date (Rayner et al. 2003) was merged with the NOAA-Optimal Interpolation version 2 analyses starting in 1981. The prescribed 1870 and 2000 SSTs and SICs from HadISST are used to estimate 1850 and 2000 conditions in the standard CESM2 component sets used here. The prescribed 2000 + 4 K annual-mean SST simulations follow the Cloud Feedback Model Intercomparison Project (CFMIP) Tier 1 amip-p4k protocol, where SSTs have been subject to a uniform 4 K warming with unchanged sea ice conditions (Bony et al. 2011), and are used to estimate future extreme conditions (Webb et al. 2017).

b. Aerosol forcing representation

Aerosol emissions are obtained from the Community Emissions Datasystem (CEDS), which contains a historical dataset of aerosol and greenhouse gas emissions from 1750 to 2014 for CMIP6 (Danabasoglu et al. 2020; Hoesly et al. 2018). Aerosol emissions are introduced from the surface through the emission of sulfate, black carbon, primary organic matter, dust, sea salt, and secondary organic aerosol (Danabasoglu et al. 2020), though some sulfate emissions are injected vertically and are fully interactive in the model's meteorology and chemistry. An updated CAM6 aerosol scheme, Modal Aerosol Model, version 4 (MAM4), is used, which includes a primary carbon aerosol mode in addition to the MAM3 accumulation, Aitken, and coarse modes, which increases the lifetime and burdens of black carbon and primary organic matter in CAM6 (Liu et al. 2016; Emmons et al. 2020).

c. Aerosol indirect effect and cloud representation in CAM6

CAM6, used as the atmospheric component of the simulations in this study, uses the CLUBB high-order turbulence closure (Danabasoglu et al. 2020). CLUBB uses the updated MG2 microphysics scheme that was specifically developed to address the overestimated aerosol sensitivity in GCMs by including prognostic precipitation processes, liquid and ice number concentrations, and liquid and ice mixing ratios (Gettelman et al. 2015, 2008). In MG2, convective clouds are treated with single-moment microphysics, and large-scale stratiform clouds are treated with detailed, bulk double-moment parameterizations of number concentration and mixing ratio, which includes subgrid cloud water distribution (Morrison and Gettelman 2008). These detailed treatments of the stratiform parameterizations in MG2 lead to improved aerosol–cloud interactions in all boundary layer clouds in CLUBB. Mixed-phase and ice nucleation parameterizations dependent on both temperature and aerosol interactions are added separately into CAM6, resulting in aerosol–cloud interactions in boundary layer, mixed-phase, and ice clouds in CAM6 (Hoose et al. 2010; Wang et al. 2014; Shi et al. 2015; Gettelman and Morrison 2015; Gettelman et al. 2015; Morrison and Gettelman 2008). The implementation of CLUBB in CAM6 produces thicker low clouds that agree better with observations (Bogenschutz et al. 2013), reducing biases in shallow cumulus and stratocumulus regimes and in low cloud globally. However, there are slight overestimations of cloud amount in the lower troposphere (Bogenschutz et al. 2013). CLUBB also reduces biases in the shortwave cloud forcing (SWCF) in storm-track regions and over continental deep convective regions, but the thicker clouds simulated in CLUBB can lead to an overestimation of SWCF in the Northern Hemisphere Pacific stratus region (Bogenschutz et al. 2013). MG2 also shows a stronger SWCF and longwave cloud forcing (LWCF) in storm tracks and the tropics, but the cloud forcing is too strong globally when compared to observations (Gettelman et al. 2015). The implementation of CLUBB did not improve high cloud representation or the LWCF that is dominated by these high clouds, which is still a persistent bias in CAM (Bogenschutz et al. 2013). However, the ice nucleation parameterizations implemented separately in CAM6 allow for more realistic aerosol–cloud interactions in high clouds though still limited by the lack of observational data on which to base these parameterizations (Hoose et al. 2010; Shi et al. 2015).

The aerosol–cloud interactions were found to be sensitive to the prognostic precipitation implemented in MG2, which slightly lowered the global aerosol–cloud interactions, with predominant decreases in the tropics near Southeast Asia (Gettelman et al. 2015). The representation of colder regions of the planet in MG2 is still a persistent issue, which could greatly impact the total cloud feedback and climate sensitivity (Gettelman et al. 2015). Although there have been great improvements in the prognostic precipitation, accretion to autoconversion ratios, and microphysical process rates in MG2, it is important to recognize the mixed-phase and ice biases that might occur from the lack of representation in this stratiform scheme, despite ice nucleation being implemented separately into CAM6.

d. Experimental design

We conduct six different repeating annual cycle prescribed SST simulations in CESM2 as part of this study: 1850 SSTs and other natural and nonaerosol anthropogenic forcings with 1850 anthropogenic aerosol emissions (SST1850_Aero1850), 1850 SSTs and other natural and nonaerosol anthropogenic forcings with 2000 anthropogenic aerosol emissions (SST1850_Aero2000), 2000 SSTs and other natural and nonaerosol anthropogenic forcings with 1850 anthropogenic aerosol emissions (SST2000_Aero1850), 2000 SSTs and other natural and nonaerosol anthropogenic forcings with 2000 anthropogenic aerosol emissions (SST2000_Aero2000), 2000 + 4 K SSTs and 2000 natural and nonaerosol anthropogenic forcings with 1850 anthropogenic aerosol emissions (SST + 4 K_Aero1850), and 2000 + 4 K SSTs and 2000 natural and nonaerosol anthropogenic forcings with 2000 anthropogenic aerosol emissions (SST + 4 K_Aero2000). It is important to note that the natural and anthropogenic forcings used in the 2000 + 4 K simulations do not reflect those of a 4 K warmer state and are fixed using the 2000 conditions from the standard CESM2 component sets. The differences between each of these simulations isolate various effects or responses in the simulations and have been named accordingly, summarized in Table 1. These simulations are designed to capture the effect of aerosol forcing in a preindustrial, present-day, and idealized extremely warmed climate in which both SSTs and nonanthropogenic aerosol atmospheric composition (e.g., greenhouse gas concentrations) are modified. Cloud changes captured between the PI and other background climates (i.e., in ΔBC2000) thus include both cloud responses to SST changes and cloud adjustments to in situ atmospheric forcing differences. Experiment setup follows the protocol used in the Radiative Forcing Model Intercomparison Project (RFMIP) and widely across the literature (Smith et al. 2020; Persad and Caldeira 2018; Persad 2023).

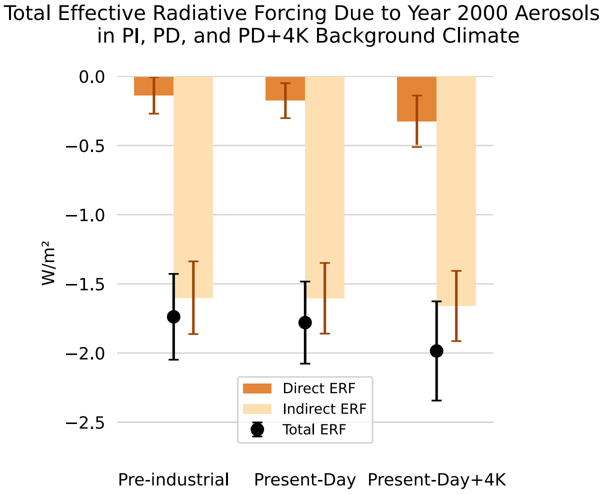

FIG. 1. The global-mean total ERF in response to year 2000 anthropogenic aerosol emissions in a preindustrial (PD1850), present-day (PD2000), and idealized extremely warm (PD + 4 K) background climate, with the direct and indirect forcing contributions for each. The small change in the effective radiative forcing in response to the year 2000 anthropogenic aerosol forcing between background climates is due to the small change in the direct forcing rather than the indirect forcing.

includes effects from other noncloud feedbacks like the Planck and water vapor feedbacks (Soden et al. 2004).

f. Statistical significance calculations

To calculate the statistical significance between variable differences in this study, Welch's unequal variances *t* test with a 90% confidence level is used, where the population density functions are populated by the means from the individual 40 years of the equilibrated average. The 90% confidence interval is noted in the bottom-left corner of the global maps with stippling, indicating changes that are not significant.

3. Results

a. Aerosol effective radiative forcing estimation under different background climates

Contrary to our initial hypothesis, we find that the AIE is not dependent on the background climate state in these idealized CESM2 CAM6 simulations in the global mean. The ΔPD2000, which captures how the year 2000 aerosol forcing changes between preindustrial and present-day background climates, produces a global-mean decrease in ERF of only −0.042 ± 0.398 W m^{-2} (Figs. 1 and 2a). The PD1850, which captures the effect of year 2000 aerosol emissions in a preindustrial climate, produces a global-mean ERF of −1.74 ± 0.310 W m^{-2}, which can be decomposed into a direct forcing of −0.14 ± 0.132 W m^{-2} and an indirect forcing of −1.60 ± 0.263 W m^{-2} (Fig. 1, supplemental Figs. 1a–c). The PD2000, which captures the effect of year 2000 aerosol emissions in a present-day climate, produces a global-mean ERF of −1.78 ± 0.297 W m^{-2}, which can be decomposed into a direct forcing of −0.18 ± 0.126 W m^{-2} and an indirect forcing of −1.60 ± 0.255 W m^{-2} (Fig. 1, supplemental Figs. 1d–f). The ΔPD + 4 K, which captures how the year 2000 aerosol forcing changes between preindustrial and extreme background climates, produces a global-mean decrease in ERF of −0.25 ± 0.436 W m^{-2} (Figs. 1 and 2d). The PD + 4 K, which captures the effect of year 2000 aerosol emissions in an extreme climate, produces a global-mean ERF of −1.99 ± 0.359 W m^{-2}, which can be decomposed into a direct forcing of −0.33 ± 0.186 W m^{-2} and an

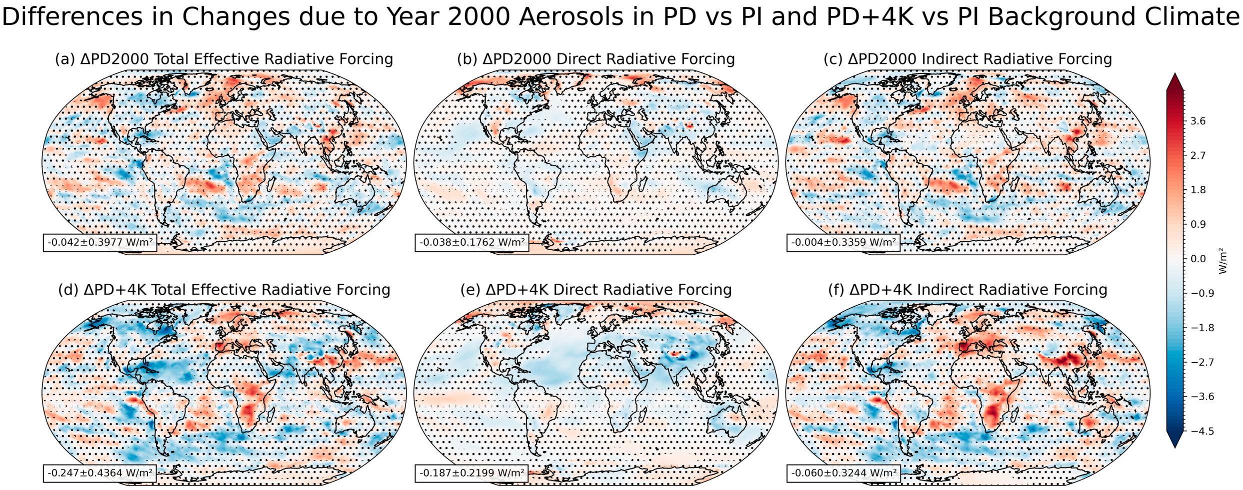

FIG. 2. The spatial distribution of the differences in changes in (a) the total effective radiative forcing, (b) direct forcing, and (c) indirect forcing due to present-day aerosol emissions imposed in a present-day vs a preindustrial background climate (ΔPD2000), and (d) total effective radiative forcing, (e) direct forcing, and (f) indirect forcing due to present-day aerosol emissions imposed in an idealized extremely warm vs a preindustrial background climate (ΔPD + 4 K). The global means with 90% confidence intervals for each are noted in the bottom-left corner. Stippling indicates changes that are not significant. The small changes in the effective radiative forcing come from the changes in the direct forcing and not the indirect forcing.

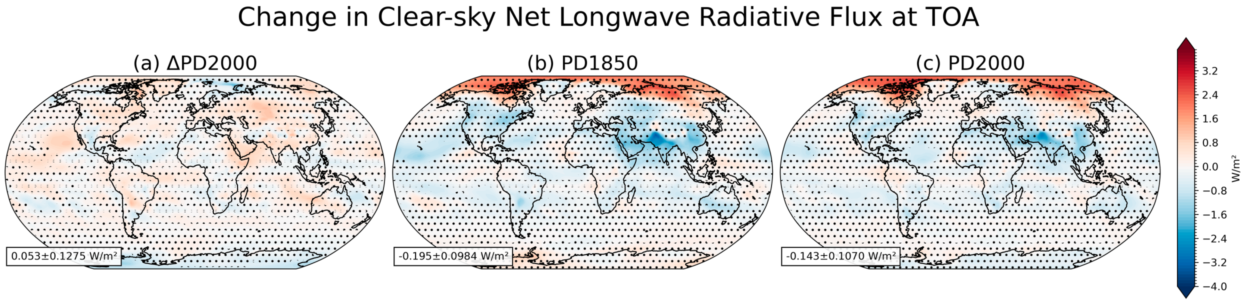

FIG. 3. The spatial distribution of the clear-sky net longwave radiative flux at top of atmosphere (TOA) in (a) ΔPD2000 (differences in changes in PD1850 vs PD2000), (b) PD1850 (changes due to present-day aerosols in PI background climate), and (c) PD2000 (changes due to present-day aerosols in PD background climate). The global means with 90% confidence intervals for each are noted in the bottom-left corner. Stippling indicates changes that are not significant. The small and insignificant change in direct forcing in ΔPD2000 is driven largely by the OLR in ΔPD2000, which is due to the increased trapping of the upwelling longwave radiation in the atmosphere from year 2000 greenhouse gases in PD2000, leading to weaker changes in OLR at TOA than in PD1850.

indirect forcing of -1.66 ± 0.254 W m^{-2} (Fig. 1, supplemental Figs. 1g–i). These results show that the small and statistically insignificant decrease in total ERF in ΔPD2000 and ΔPD + 4 K comes from the statistically insignificant decrease in the direct forcing of -0.04 ± 0.176 W m^{-2} in ΔPD2000 and -0.19 ± 0.220 W m^{-2} in ΔPD + 4 K and not from the indirect forcing as hypothesized (Fig. 2).

b. *Aerosol direct radiative forcing under different background climates*

The statistically insignificant decrease in direct forcing in ΔPD2000 (Figs. 1 and 2b) and ΔPD + 4 K (Figs. 1 and 2e) can be decomposed into the net shortwave (not shown) and longwave components but are largely driven by the longwave components. Note that the small increase in direct forcing near the sea ice boundary in ΔPD2000, contrary to the expectation of sea ice loss with warming, is due to a liquid-to-solid precipitation transition in the Arctic region due to year 2000 aerosol emissions (Pan et al. 2020; supplemental Figs. 11a,b), thereby increasing the surface albedo (supplemental Figs. 10a,b) of sea ice coverage, manifesting as an increase in the direct forcing. The outgoing longwave radiation (OLR) components show a global-mean increase of 0.05 ± 0.128 W m^{-2} in ΔPD2000 (Fig. 3a) and 0.13 ± 0.165 W m^{-2} in ΔPD + 4 K (supplemental Fig. 2c) (positive upward). To investigate this increase in net OLR, i.e., cooling, in ΔPD2000 further, we look at the individual differences in OLR in PD1850 and PD2000 (Figs. 3b,c).

There is a global-mean decrease in OLR in PD1850 of -0.20 ± 0.098 W m^{-2} (Fig. 3b) and a global-mean decrease in OLR in PD2000 of -0.14 ± 0.107 W m^{-2} (Fig. 3c). While both PD1850 and PD2000 show significant decreases in OLR due to surface cooling from the addition of year 2000 aerosol emissions, PD2000 shows a weaker decrease in OLR than PD1850. We believe this is due to the increased trapping of the upwelling longwave radiation from the surface by year 2000 greenhouse gases, which are present in PD2000 but absent in PD1850, which creates a weaker change in OLR at the TOA in response to the addition of aerosols captured in PD2000. This weaker change in OLR in PD2000 leads to an increase in OLR in ΔPD2000 since ΔPD2000 = PD2000 − PD1850 and manifests as a change in the direct forcing signal in ΔPD2000. Therefore, this small and statistically insignificant change in ΔPD2000 direct forcing is unrelated to the behavior of aerosol radiative effects between background climates but rather due to the reduction in OLR available for the aerosol cooling to reduce due to the increased trapping of upwelling longwave radiation by year 2000 greenhouse gases in PD2000.

This same mechanism manifests in ΔPD + 4 K OLR (supplemental Fig. 2c) but is further amplified due to the water vapor feedback, which dominates the statistically insignificant ΔPD + 4 K direct forcing signal (Fig. 2e, supplemental Fig. 2a). Furthermore, there is a small contribution to ΔPD + 4 K direct forcing from the shortwave component (supplemental Fig. 2b) due to a greater increase in the retained sulfate burden in PD + 4 K compared to PD2000 (supplemental Fig. 9). This likely arises from a combination of changes in wet and dry deposition rates and an increase in hygroscopic growth due to atmospheric humidification between idealized extremely warm and preindustrial background climates (ΔBC + 4 K) (not shown).

c. *Aerosol indirect radiative forcing under different background climates*

Contrary to our expectation, the difference in indirect forcing in response to year 2000 aerosol emissions between a preindustrial, present-day, and extreme background climate is negligible (-0.004 ± 0.336 and -0.06 ± 0.324 W m^{-2}, respectively; see also Figs. 1, 2c,f, supplemental Figs. 1c,f,i). One possibility is that there is regional compensation of the AIE changes in ΔPD2000 and ΔPD + 4 K, resulting in minimal global-mean change. Figure 2c shows that in addition to the statistical insignificance of the global-mean difference in ΔPD2000, there are essentially no statistically significant differences in the regional distribution. This shows that the lack of change in the ΔPD2000 indirect forcing is not due to regional cancellation.

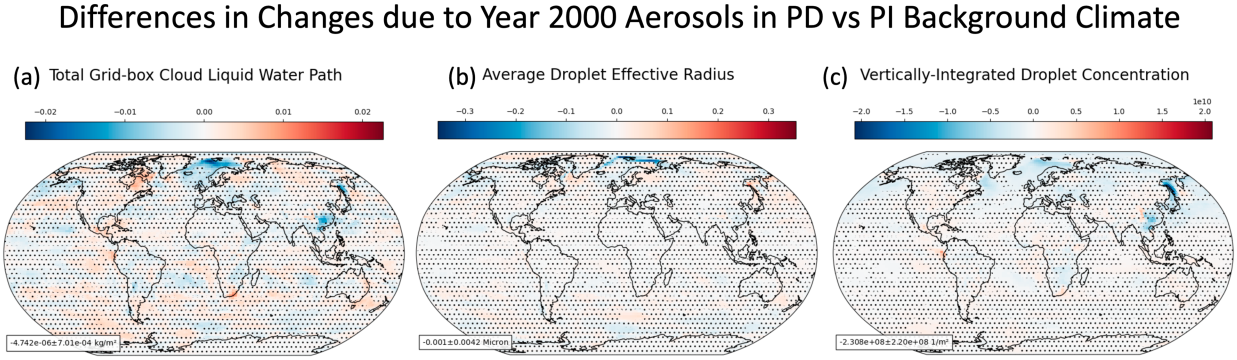

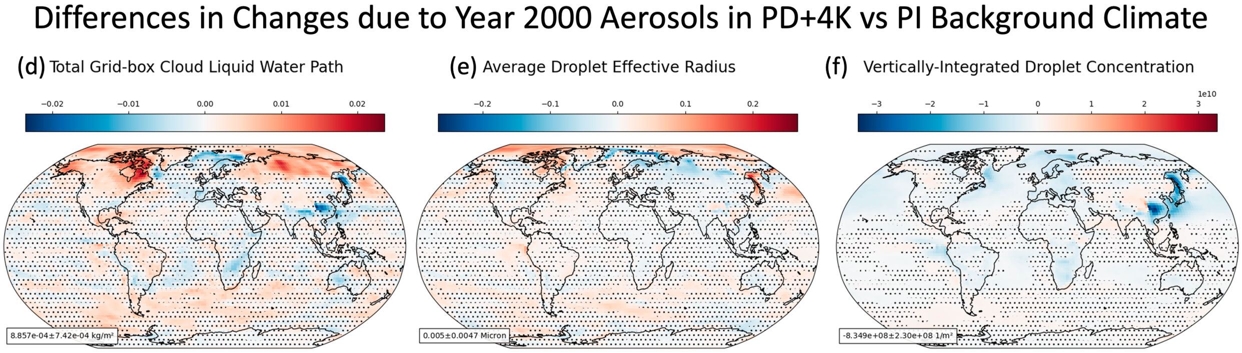

FIG. 4. The spatial distribution of the differences in changes in (a) the total gridbox cloud liquid water path (kg m^{-2}), (b) average droplet effective radius (μm), and (c) cloud droplet number concentration (1 m^{-2}) due to present-day aerosol emissions imposed in a present-day vs preindustrial background climate (ΔPD2000), and (d) total gridbox cloud liquid water path (kg m^{-2}), (e) average droplet effective radius (μm), and (f) cloud droplet number concentration (1 m^{-2}) due to present-day aerosol emissions imposed in an idealized extremely warm vs preindustrial background climate (ΔPD + 4 K). The global means with 90% confidence intervals for each are noted in the bottom-left corner. Stippling indicates changes that are not significant. There is a small decrease in the liquid water path and cloud droplet number concentration in ΔPD2000 but minimal regional changes across the variables. There are significant regional changes in the cloud liquid water path, average droplet effective radius, and cloud droplet number concentration in ΔPD + 4 K.

However, in ΔPD + 4 K, there are significant regional AIE dependencies that cancel out in the global mean. Significant increases in the ΔPD + 4 K indirect forcing in the North American Arctic and Southern Ocean (Fig. 2f) are driven by a greater liquid water path increase in response to the addition of aerosols (Fig. 4d) from greater atmospheric specific humidity in the idealized extremely warm climate (not shown). This increase in cloud liquid water path increases cloud reflectivity with the unchanged total cloud amount in these regions (supplemental Fig. 4), causing an increase in the indirect forcing regionally. Low- and midlevel cloud changes, meanwhile, drive the compensating reductions in the ΔPD + 4 K indirect forcing strength in Europe, Central, and Southern Africa, and Southeast Asia (Fig. 2f). Global decreases in low- and midlevel clouds between preindustrial and extreme background climates (ΔBC + 4 K; supplemental Figs. 8a,b) from the tropical and midlatitude low cloud amount feedbacks decrease the cloud amount available for the year 2000 aerosols to interact with. Therefore, when year 2000 aerosols are imposed in the extreme climate state, the cloud droplet number concentration increases by less than in a preindustrial climate state (supplemental Figs. 3c,i), manifesting as a decrease in the cloud droplet number concentration in ΔPD + 4 K (Fig. 4f). Nevertheless, these regionally opposing signals lead to minimal change in the global-mean AIE strength in ΔPD + 4 K.

We next investigate whether the lack of background climate dependence in indirect forcing could be due to regional, vertical, or across-variable cancellation of the microphysical variables that contribute to the net change in AIE. An increase in anthropogenic aerosols leads to more numerous and smaller cloud droplets for a given liquid water path (Twomey 1974; Bellouin et al. 2020; Forster et al. 2021), which causes other adjustments like precipitation suppression and cloud thickening that might manifest as changes in the cloud liquid water path (Albrecht 1989; Pincus and Baker 1994; Bellouin et al. 2020). Therefore, we would expect year 2000 anthropogenic aerosol emissions to alter the cloud liquid water path, cloud droplet number concentration, and droplet effective radius, which would all contribute to the net change in AIE. However, the total gridbox cloud liquid water path change in ΔPD2000 shows minimal changes in the global mean (Fig. 4a). There are small decreases in the liquid water path in the northeastern Atlantic but minimal changes elsewhere. The average droplet effective radius change in ΔPD2000 shows only a small (and statistically insignificant) decrease of −0.001 ± 0.004 μm in the global mean (Fig. 4b). The cloud droplet concentration change in ΔPD2000 shows a

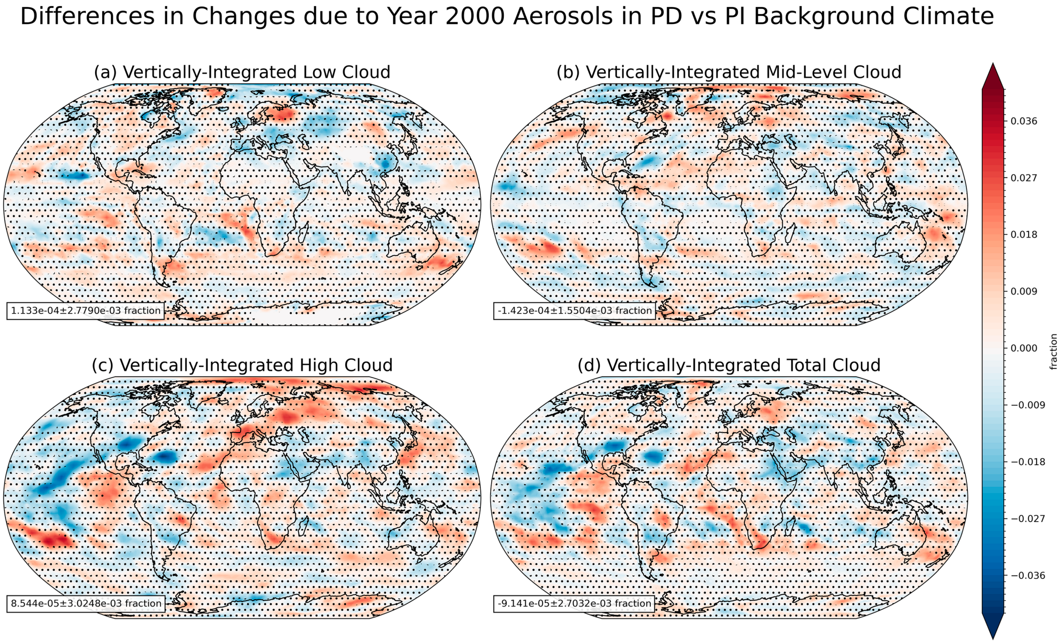

FIG. 5. The spatial distribution of the differences in changes in vertically integrated (a) low, (b) midlevel, (c) high, and (d) total cloud due to present-day aerosol emissions imposed in a present-day vs preindustrial background climate (ΔPD2000). The global means with 90% confidence intervals for each are noted in the bottom-left corner. Stippling indicates changes that are not significant. There are small significant regional differences between background climates in certain cloud regimes, but globally, there are minimal significant changes.

$-2.31 \times 10^8 \pm 2.20 \times 10^8$ 1 m^{-2} decrease in the global mean, focused in the high northern latitudes (Fig. 4c). There are regionally compensating increases in the cloud liquid water path, increases in the average droplet effective radius, and decreases in the cloud droplet number concentration across the Arctic in ΔPD + 4 K (Figs. 4d–f). Individual PD1850, PD2000, and PD + 4 K responses are shown in supplemental Fig. 3. This shows that individual microphysical variable cancellation is not responsible for the lack of change in the ΔPD2000 indirect forcing but is responsible for slight compensation in the ΔPD + 4 K indirect forcing.

Because our estimation of the indirect forcing includes cloud adjustments, a possible driver of the minimal dependence of the global-mean net AIE on background climate could come from regional or vertical compensation between different cloud amount adjustments in response to the addition of aerosols into the different background climates. Figure 5 shows the difference in low, midlevel, high, and total cloud fraction changes in ΔPD2000 (supplemental Fig. 4 for ΔPD + 4 K). There is not a statistically significant difference in the global-mean values of the low, midlevel, high, or total cloud fraction adjustments in response to aerosols between background climates. There is a slight decrease in low clouds in ΔPD2000 in the Northern Atlantic, which could be related to the decrease in the liquid water path and cloud droplet number concentration in this area (Fig. 5a). There is a slight decrease in high clouds in ΔPD2000 over the Pacific, driving the small decrease of total cloud in this region (Figs. 5c,d). The ΔPD + 4 K cloud responses have a similar spatial pattern to those of ΔPD2000 with a larger magnitude but still mostly lack significance (supplemental Fig. 4). Individual PD1850, PD2000, and PD + 4 K cloud responses are shown in supplemental Figs. 5–7. This shows that there are minimal differences in cloud adjustments in ΔPD2000 and ΔPD + 4 K and that regional or vertical compensation is not responsible for the lack of change in global-mean ΔPD2000 or ΔPD + 4 K indirect forcing.

d. Isolating background climate responses with constant aerosol emissions

There are many cloud and smaller meteorological changes that are expected with atmospheric warming (Sherwood et al. 2020; Zelinka et al. 2020; Forster et al. 2021), which we hypothesize should chiefly decrease the strength of AIE in the global mean between preindustrial and present-day climate states (see section 1). The ΔBC + 4 K cloud changes are aligned with those expected from the cloud and water vapor feedbacks discussed in section 1 (supplemental Fig. 8), which likely drive the significant regional dependence of AIE in ΔPD + 4 K, despite the compensation in the global-mean AIE signal. However, our results indicate a minimal change in the global-mean ΔPD2000 AIE and no such regionally significant signals. The final possible explanation we explore is that the expected dominant decrease in tropical high, tropical marine low, and subtropical marine low clouds between a preindustrial and present-day climate that our hypothesis of AIE dependence is based on might not be present in our PD simulations. Below, we present the horizontal distribution, vertical distribution, magnitude, and phase of the cloud responses

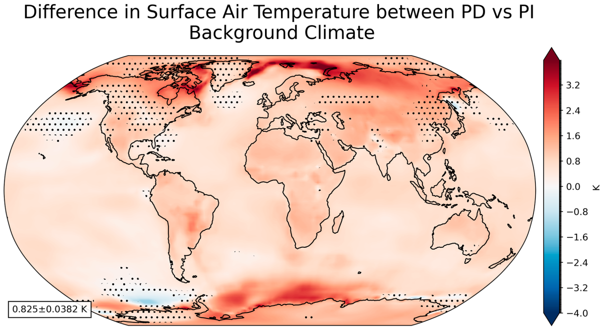

FIG. 6. The spatial distribution of the difference in surface air temperature between a present-day and preindustrial background climate with constant preindustrial aerosol emissions (ΔBC2000). The global mean with a 90% confidence interval is noted in the bottom-left corner. Stippling indicates changes that are not significant. As expected, there is a global-mean surface air temperature increase from a preindustrial to a present-day background climate of ~0.83 K, with greater warming in the high latitudes.

with constant anthropogenic aerosol emissions but changing SSTs, SICs, and all other forcings, between a preindustrial and present-day background climate state, ΔBC2000. In section 4, we assess how those background climate changes in ΔBC2000 align with the expectations proposed in the introduction (section 1).

The ΔBC2000 produces 0.83 ± 0.038 K of the global-mean surface warming, as expected based on observations of the global-mean temperature change between (1859–1900) and (1995–2014) (Fig. 6) (Eyring et al. 2021). The ΔBC2000 produces a global-mean decrease in the CRE (positive downward) of −0.72 ± 0.235 W m^{-2} in response to this greenhouse gas warming (Fig. 7a), which varies from the CRE expected with 0.83 K of surface warming (Forster et al. 2021). In many areas, there is increased cloud reflectivity in response to nonaerosol changes from preindustrial to present-day, contrary to the expected dominant radiative response from decreasing tropical and subtropical marine low clouds (Fig. 7a) (Sherwood et al. 2020; Zelinka et al. 2020; Forster et al. 2021). This global-mean decrease in CRE can be decomposed into the counteracting shortwave and longwave cloudy-sky radiative fluxes in ΔBC2000 (Figs. 7b,c). The global-mean shortwave component of the CRE (positive downward) in ΔBC2000 shows an increase of 0.18 ± 0.254 W m^{-2} (Fig. 7b), implying less shortwave reflectivity in a present-day climate than a preindustrial climate. This is to be expected based on the decrease of low clouds globally with greenhouse gas warming (Forster et al. 2021; Sherwood et al. 2020; Boucher et al. 2013). However, the global-mean longwave component of the CRE (positive upward) in ΔBC2000 shows an increase of 0.90 ± 0.077 W m^{-2} (Fig. 7c), implying more outgoing longwave radiation due to cloud changes in a present-day climate than in a preindustrial climate. This is contrary to the expected high cloud altitude feedback response (Forster et al. 2021; Zelinka and Hartmann 2010; Hartmann and Larson 2002) but in line with the findings of Raghuraman et al. (2023), which find that the current increase in the observed longwave CRE is due to clouds masking the reduction in OLR from greenhouse gases in all-sky conditions (Raghuraman et al. 2023).

The shortwave and longwave components of the CRE can be broken down further into individual cloud changes between background climates to investigate what cloud regimes might be driving the increased outgoing shortwave and longwave radiation. The low, midlevel, high, and total cloud changes in ΔBC2000 are shown in Fig. 8. The ΔBC2000 produces decreases in high clouds across the tropics globally (Fig. 8c), correlating with the small decreases in tropical high clouds expected with greenhouse gas warming (Forster et al. 2021). Furthermore, there are larger increases in high clouds of ~0.06 fraction over Antarctica and ~0.02 fraction over the Arctic. Cloud-top height increases in the global mean (not shown), in line with the FAT hypothesis (Forster et al. 2021; Zelinka and Hartmann 2010; Hartmann and Larson 2002). However, many of the tropical and high-latitude high cloud responses are damped by the midlevel and low cloud responses in the total cloud signal (Fig. 8).

The phase of cloud water could greatly impact the reflectivity of the clouds present, influencing the total CRE (Bjordal et al. 2020; Tan et al. 2016; Forster et al. 2021). The ΔBC2000 spatial distribution of total gridbox liquid water path responses

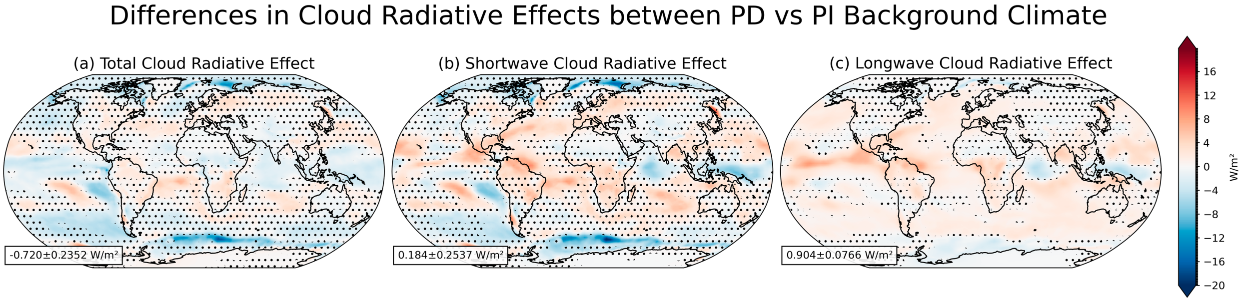

FIG. 7. The spatial distribution of the differences in (a) total (positive downward), (b) shortwave (positive downward), and (c) longwave (positive upward) cloud radiative effects between a present-day vs preindustrial background climate with constant preindustrial aerosol emissions (ΔBC2000). The global means with the 90% confidence intervals for each are noted in the bottom-left corner. Stippling indicates changes that are not significant. There is a global-mean negative total cloud radiative effect, with larger negative regions in the Pacific Ocean. The increased outgoing longwave radiation between present-day and preindustrial background climates is the leading contributor to the decreased cloud radiative effect between background climates.

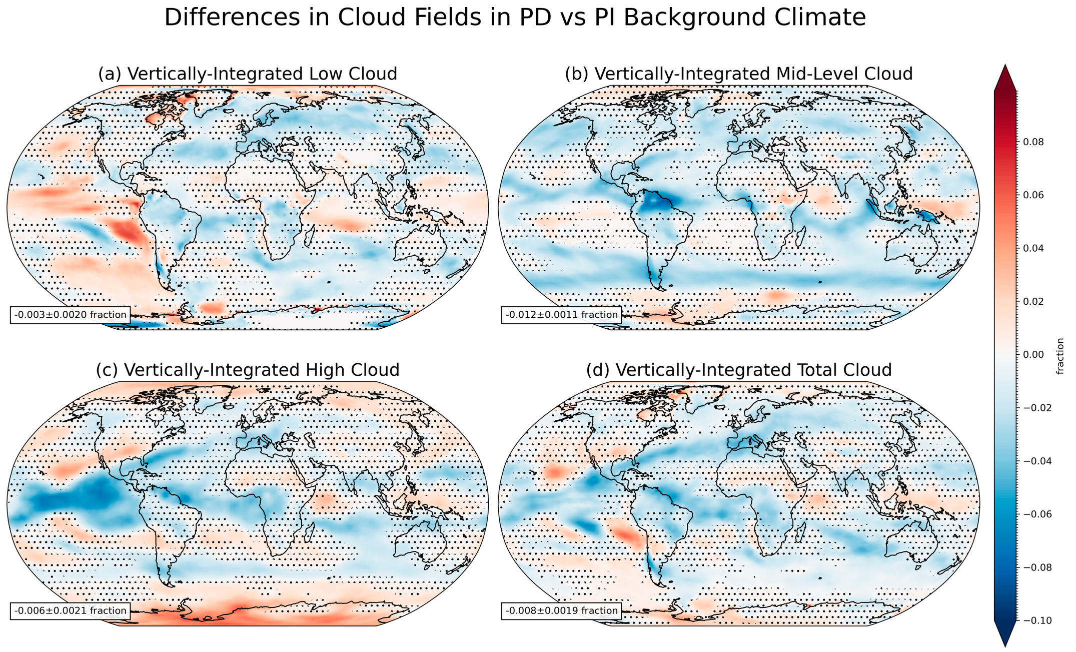

FIG. 8. The spatial distribution of the differences in vertically integrated (a) low, (b) midlevel, (c) high, and (d) total clouds between a present-day vs preindustrial background climate with constant preindustrial aerosol emissions (ΔBC2000). The global means with 90% confidence intervals for each are noted in the bottom-left corner. Stippling indicates changes that are not significant. The large-scale decreases across the tropics at midlevel and high altitudes dominate the total cloud response, but the increase in low clouds over the Pacific Ocean slightly compensates for this.

correlates strongly with the ΔBC2000 spatial distribution of total cloud water path responses, seen also in the similarity of the global means, supporting the interpretation that the cloud liquid water path responses are the dominant drivers of the total cloud water path changes in ΔBC2000 (Fig. 9). There are a few areas that show a transition from ice water path to liquid water path with unchanged total water path, but these are negligible in comparison to the global increase of the cloud liquid water path. Hence, the expected small extratropical phase change feedback might not be present in these simulations or might be heavily outweighed by other atmospheric changes.

4. Discussion

Given the expected decrease in tropical and subtropical marine low clouds (Forster et al. 2021; Sherwood et al. 2020; Boucher et al. 2013), rise in high cloud tops (Zelinka and Hartmann 2010; Hartmann and Larson 2002), and phase change of extratropical clouds (Bjordal et al. 2020; Tan et al. 2016; Forster et al. 2021) with warming that dominate the cloud responses in ΔBC + 4 K (supplemental Fig. 8) and drive regional dependencies of AIE in ΔPD + 4 K (Fig. 2f) that compensate in the global mean, the absence of expected AIE and cloud dependence on background climate in ΔPD2000 requires explanation. The lack of dependence of AIE in the global mean

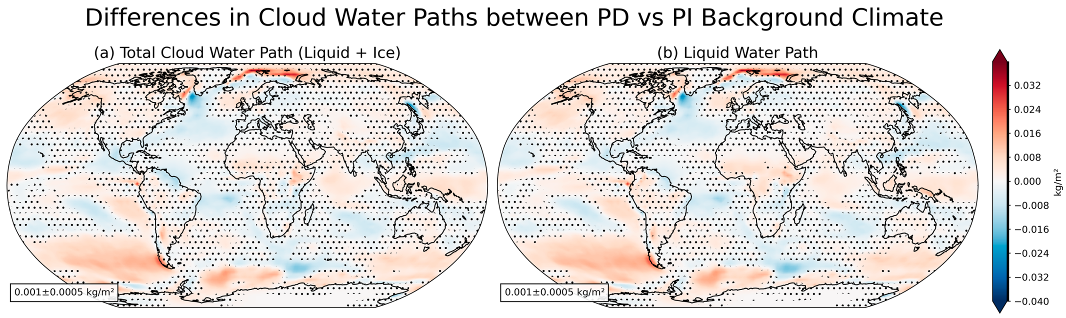

FIG. 9. The spatial distribution of the differences in vertically integrated total gridbox (a) cloud water path (liquid + ice) and (b) liquid water path between a present-day vs preindustrial background climate with constant preindustrial aerosol emissions (ΔBC2000). The global means with the 90% confidence intervals for each are noted in the bottom-left corner. Stippling indicates changes that are not significant. This shows that the changes in the cloud liquid water path dominate the total cloud water path changes.

with 0.83 ± 0.038 K (Fig. 6) of surface warming between our simulations could be understandable, given the small contributions of the tropical (+0.25 ± 0.16 W m^{-2} K^{-1}) and midlatitude (+0.12 ± 0.12 W m^{-2} K^{-1}) marine low cloud, high cloud altitude (+0.20 ± 0.10 W m^{-2} K^{-1}), and cloud optical depth (0.0 ± −0.10 W m^{-2} K^{-1}) feedbacks to the TOA flux per degree kelvin of warming (Sherwood et al. 2020). However, the lack of regional dependence, given the collocation of the spatially heterogeneous changes in aerosol emissions and cloud regimes in these simulations, warrants further investigation. We explore three potential explanations below: (i) cancelling signals across different AIE variables (section 3c), (ii) cancelling signals of cloud amount adjustments (section 3d), and (iii) unexpected cloud responses to change in background climate (section 3e).

AIE strength could appear independent of background climate due to the cancellation between the individual microphysical variables that make up the total AIE, such as cloud droplet number concentration and droplet effective radius. Cancellation could occur regionally, vertically, or across variables, which in combination could lead to minimal change in the global mean and regional AIE (see section 3c) that does occur in the Arctic region of ΔPD + 4 K (Figs. 4d–f). However, Fig. 4 shows minimal changes in the ΔPD2000 cloud liquid water path, cloud droplet number concentration, and average droplet effective radius—the major variables that contribute to total AIE. These do not cancel each other out regionally or across variables. Therefore, regional, vertical, or cross-variable compensation in microphysical determinants of AIE strength does not explain the lack of AIE dependence in ΔPD2000.

We next assess the role of compensation across the ΔPD2000 cloud amount adjustments spatially or vertically (see section 3d). When the total cloud regime is broken down into the low, midlevel, and high cloud amounts, there are a few significant large-scale changes in both ΔPD2000 (Fig. 5) and ΔPD + 4 K (supplementary Fig. 4). While there could be some minor regional and vertical cancellations, the cloud amount adjustments are relatively insignificant. For cloud cancellation to explain the lack of AIE dependence in ΔPD2000, we would also expect cancellation in the cloud liquid water path, cloud droplet number concentration, and droplet effective radius since these are greatly influenced by large-scale cloud adjustments. Given minimal cancellation in microphysical variables and in the low, midlevel, and high cloud variables, compensation across the ΔPD2000 cloud distributions cannot explain the minimal change in the AIE in ΔPD2000.

Finally, unexpected meteorological responses between background climates could generate AIE responses contrary to what the existing literature would suggest. While the background cloud responses in ΔBC + 4 K align with those expected from the existing cloud feedback literature, likely driving the regional AIE dependencies in ΔPD + 4 K, we further investigate the ΔBC2000 atmospheric and cloud responses to identify the influences of greenhouse gas warming with constant preindustrial aerosol emissions for explanation of the minimal global-mean AIE dependence in ΔPD2000 (see section 3e).

Despite the expected positive change in CRE in response to greenhouse gas warming (Sherwood et al. 2020; Zelinka et al. 2020; Forster et al. 2021), Fig. 7a shows a global-mean negative change in the CRE in ΔBC2000 dominated by increased outgoing radiation in the Pacific. Figure 7b shows an expected shortwave-driven increase in CRE with greenhouse gas warming due to reduced marine boundary layer clouds and associated reduced shortwave reflectivity (Forster et al. 2021; Sherwood et al. 2020; Boucher et al. 2013). However, Fig. 7c does not show the expected longwave-driven increase in CRE from the rising altitude of tropical high clouds and high cloud greenhouse effect (Forster et al. 2021; Zelinka and Hartmann 2010; Hartmann and Larson 2002). Instead, more longwave radiation escapes in the present-day climate compared to the preindustrial climate, in line with the current observed increase in longwave CRE due to clouds masking the reduction in OLR from greenhouse gases in all-sky conditions (Raghuraman et al. 2023), generating the negative CRE change seen in ΔBC2000. There is a small change in high cloud altitude, consistent with the FAT hypothesis (not shown). However, the significant decrease in high and midlevel clouds (Fig. 8) dominates the increased outgoing longwave radiation in the tropics in ΔBC2000, reducing CRE, consistent with observations (Loeb et al. 2024; Raghuraman et al. 2024).

The positive tropical and subtropical marine low cloud feedback was expected to be the dominant cloud response to greenhouse gas warming (Forster et al. 2021; Sherwood et al. 2020; Boucher et al. 2013), seen in ΔBC + 4 K, but absent in ΔBC2000. While there is a small global-mean decrease in low clouds in ΔBC2000, there is a significant increase in the eastern Pacific stratocumulus regime (Fig. 8a). Although the linearly combined midlevel and low cloud changes (not shown) explain the majority of the ΔBC2000 shortwave radiation response seen in Fig. 7b, the significant increase in eastern Pacific low clouds in ΔBC2000 warrants further investigation.

To understand why the ΔBC2000 Pacific low cloud responses do not align with expected low cloud decreases with greenhouse gas-driven warming, we compared these with the CESM2 fully coupled large ensemble (LENS2) results (Rodgers et al. 2021) (Fig. 10). A possible explanation for the unexpected increases in eastern Pacific low clouds in ΔBC2000 could be that the observed SSTs imposed in ΔBC2000 are outside of the range of SSTs generated by the fully coupled models on which our expectations around cloud responses to warming were based. This discrepancy between the current observed and CMIP6 model-generated SSTs and the resulting influence on models' simulation of Pacific Walker circulation and Pacific low cloud cover, termed the pattern effect, is an area of considerable concern in the coupled model representation of responses to warming (e.g., Rugenstein et al. 2023; Wills et al. 2022; Seager et al. 2022; Dong et al. 2019; Ceppi and Gregory 2017; Zhou et al. 2017). The ΔBC2000 signal is derived from atmosphere-only simulations with prescribed observed preindustrial (year 1850) and present-day (year 2000) SSTs and SICs, whereas the LENS2 simulations have been forced with model-generated SSTs and SICs.

Recent observations of the Pacific SST distribution, also captured in ΔBC2000, show an enhanced tropical Pacific east–west SST gradient with greater warming near Australia and Japan (Forster et al. 2021; Wills et al. 2022), thereby decreasing tropospheric lapse rates across the Pacific and increasing

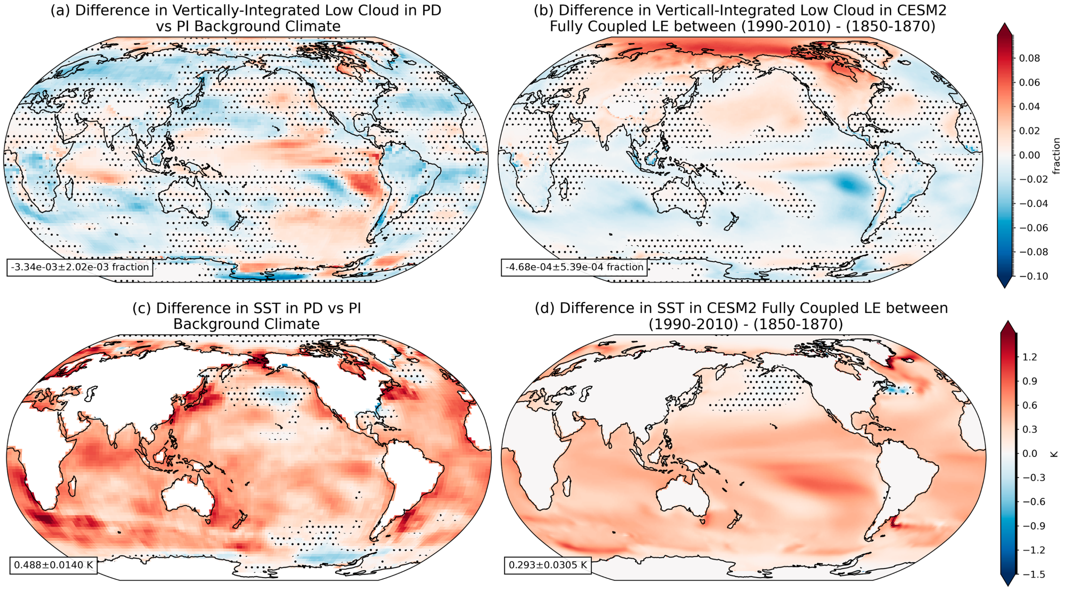

FIG. 10. The spatial distribution of the differences in (a) vertically integrated low cloud between a present-day and preindustrial background climate with constant preindustrial aerosol emissions (ΔBC2000). (c) The spatial distribution of the differences between the observed year 2000 and year 1870 SSTs used to drive the present-day and preindustrial background climate simulations in this study (ΔBC2000). The spatial distribution of the differences in 20-member CESM2 large-ensemble (b) vertically integrated low cloud and (d) SST between a 1990 and 2010 average (cf. present-day) and 1850–70 average (cf. preindustrial) climate states with aerosol emissions from the given time periods. The global means with 90% confidence intervals for each are noted in the bottom-left corner. Stippling indicates changes that are not significant. Although there is a global-mean decrease in low clouds and increase in SST in both simulation scenarios, there are increases (decreases) in low clouds in the eastern Pacific and increases in SSTs in the western (eastern) Pacific in our simulations (LENS2).

the low stratocumulus cloud formation in the eastern Pacific (Forster et al. 2021) (Figs. 10a,c). Western Pacific SST warming leads to a significantly more outgoing longwave radiation in the tropical Pacific than eastern Pacific SST warming, which could explain the dominant OLR pattern in ΔBC2000 (Dong et al. 2019). Contrary to this, LENS2 and current CMIP6 model-generated Pacific SST distributions from which most cloud feedback studies are derived show a weaker tropical Pacific east–west SST gradient with more warming of the eastern Pacific (Forster et al. 2021; Wills et al. 2022), thereby weakening Pacific Walker circulation and decreasing eastern Pacific low stratocumulus cloud formation (Forster et al. 2021) (Figs. 10b,d). The opposing tropical Pacific SST gradient between the observed and model-generated SSTs in ΔBC2000 and LENS2, respectively, drives opposite low cloud responses in ΔBC2000 than previously hypothesized from the tropical and subtropical marine low cloud feedback, which would alter the ΔBC2000 AIE responses in the dominant eastern Pacific stratocumulus decks and in the global mean. The presence of the expected dominant cloud feedbacks in ΔBC + 4 K and absence in ΔBC2000 is likely because the globally homogenous extreme warming in ΔBC + 4 K outweighs the effects of a variable Pacific east–west SST gradient that arises from the relatively smaller temperature perturbations to this gradient spread (ΔBC2000).

Other studies in the CESM2 model suite support the absence of a dependence of AIE strength on background climate, contrary to the expectation from cloud responses to warming. Simpson et al. (2023) found that the diverging near-surface air temperature projections in response to the anthropogenic aerosol forcing in the single forcing large ensembles of CESM1 and CESM2 using the “single-forcing” or “all-but-one” methodologies were due to state dependence of the ice–albedo feedback and nonlinearities in the Atlantic meridional overturning circulation (AMOC) and not due to AIE, which would have manifested in the downwelling shortwave radiation (Simpson et al. 2023). However, this did not rule out our initial hypothesis due to the complexity of the transient, fully coupled simulations and other possible confounding factors in Simpson et al. (2023), which did not explore mechanisms behind this lack of AIE dependence. Because our study asks a larger question of the dependence of AIE on the background climate state based on first principles of cloud and AIE responses to warming, we force our atmosphere-only simulations with observed SSTs, allowing us to investigate this broadly.

Here, we only assess up to the forcing, but the ERFs from year 2000 aerosols slightly vary spatially between preindustrial, present-day, and idealized extremely warm climate states. Past studies show that different spatial patterns of ERF may have different efficacies in driving global temperature responses (Persad and Caldeira 2018; Shindell and Faluvegi 2009). Hence, future studies that assess the relative efficacies of these slightly spatially varying ERFs could be useful in determining whether there are resulting dependencies in global or regional temperature response, even in the absence of dependencies in global-mean ERF. These results are also valuable for informing future experiment protocols undertaken within major Model Intercomparison Projects (MIPs), such as Cloud Feedback MIP (CFMIP) (Webb et al. 2017) and Radiative Forcing MIP (RFMIP) (Smith et al. 2020), given the presence or absence of individual cloud feedbacks and AIE dependence that does not scale linearly with the magnitude of background temperature change across all variables.

It is important to recognize certain caveats when assessing these results. CESM2 is the only model used here, but testing this hypothesis across other CMIP6 models would be insightful, given the spread of AIE across these models (Gettelman et al. 2019; Wang et al. 2021). Though CESM2's representation of aerosol–cloud interactions performs well in comparison with other CMIP6 models, there are still biases in the microphysical parameterizations and cloud representations, which could bias the AIE in this model and these simulations (Danabasoglu et al. 2020; Gettelman et al. 2019).

The years 1850 and 2000 were chosen arbitrarily for this study to represent preindustrial and present-day climate states. However, model representation of an accurate 1850 preindustrial climate is difficult due to the lack of accurate SST records. Following CESM2 standard protocols, Hadley/NOAA-OI SSTs used to force our 1850 idealized climate are from the year 1870 (Rayner et al. 2003). Additionally, the observed year 2000 SSTs used to represent our present-day climate was a La Niña year (NOAA Climate Prediction Center). Since there are no ensemble or model means to separate this internal variability from the dominant climate signal, the enhanced tropical Pacific SST gradient present in the 2000 SSTs could modify the base state used to represent the present-day climate in these simulations. Therefore, the presence or absence of an AIE dependence on background climate assessed in these idealized simulations could be variable based on the state of climate variability. However, if the particular mode of variability is the driver of the lack of AIE dependence found in these simulations, this suggests that for at least some dominant modes of natural variability, the forced signal is not capable of producing an AIE dependence on the background climate state.

5. Conclusions

We have investigated the dependence of the AIE on the background climate state in CESM2 CAM6 using fixed-SST equilibrium simulations that represent preindustrial, present-day, and idealized extremely warm background climates with preindustrial and present-day anthropogenic aerosol emissions. Contrary to our initial hypothesis of weakened AIE in a present-day background climate due to declining marine stratocumulus clouds and despite CESM2's strong aerosol–cloud interactions, we do not find a dependence of AIE on the background climate state between preindustrial and present-day simulations but do find compensating regional dependencies between preindustrial and idealized extremely warm climate states. Driven by the homogeneous extreme warming in an idealized warm climate state, global cloud reductions dampen the increase in the cloud droplet number concentration from present-day aerosol emissions in an extreme climate state, decreasing AIE in ΔPD + 4 K regionally, which is compensated by the regional increases in AIE in ΔPD + 4 K from the increased cloud liquid water path due to atmospheric humidification. We find a small increase in the global-mean ERF in ΔPD2000 and ΔPD + 4 K due to the trapping of upwelling longwave radiation in the atmosphere from year 2000 greenhouse gases imposed in the present-day experiments, further amplified by the water vapor feedback in ΔPD + 4 K and a greater retained sulfate burden. Upon investigation of the expected dominant reduction in marine stratocumulus clouds over the eastern Pacific between background climates, which is present in an idealized extremely warm climate state but absent in a present-day climate state, we find an increase in low clouds in this region in the present-day background climate, which we attribute to the manifestation of the pattern effect in our simulations. When compared with LENS2 simulations from similar periods, we find opposite low cloud and SST responses in the eastern Pacific region, which could be due to the known disagreement in observed and model-generated SSTs used to force our simulations and the LENS2 simulations, respectively. These differences in SST patterns, particularly in the tropical Pacific, modify the strength of Walker circulation and cause differing low cloud responses in the eastern Pacific, leading to unexpected AIE responses (or rather lack thereof) between climate states. This highlights the wide-ranging impacts of the pattern effect.

It should be noted that despite the influence of the pattern effect, there is still an SST pattern and strength difference between our preindustrial and present-day simulations, even if not the expected forced one. Thus, we would expect meteorological changes between the two climate states that could affect AIE strength based on first principles, as discussed in section 1. Therefore, the lack of dependence of the AIE strength on the background climate state in these simulations is still contrary to our initial hypothesis and merits further investigation.

The results of this study indicate that AIE strength may not have a strong dependence on the present-day background climate state but could show regional dependencies in an idealized extremely warm climate. This suggests that conclusions drawn about AIE strength based on historical observations can be expected to hold as climate warms and that differing AIE strengths are unlikely to be a major concern in single-forcing experiment design (Simpson et al. 2023; Smith et al. 2022). However, additional research is needed to assess whether this finding continues to hold across a range of model implementations and states of natural variability.

Acknowledgments. We thank the reviewers for the helpful comments on this study and the University of Texas at Austin's Texas Advanced Computing Center (TACC) for the computing time. This work is partially supported by the National Science Foundation's Climate and Large-Scale Dynamics program under Award 2235177. The NCAR LENS2 simulations analyzed in this study are from the CESM2 Large Ensemble Community Project (LENS2), supported

by the IBS Center for Climate Physics in South Korea, with documentation by Rodgers et al. (2021).

Data availability statement. Input data files are available as part of the open-source public release of NCAR CESM2, available at https://www.cesm.ucar.edu/models/cesm2 [University Corporation for Atmospheric Research (UCAR), 2018]. All output data analyzed in this study are citable and available for download through the Texas Data Repository at https://doi.org/10.18738/T8/PNEI6T.

REFERENCES

Albrecht, B. A., 1989: Aerosols, cloud microphysics, and fractional cloudiness. *Science*, **245**, 1227–1230, https://doi.org/10.1126/science.245.4923.1227.

Bellouin, N., and Coauthors, 2020: Bounding global aerosol radiative forcing of climate change. *Rev. Geophys.*, **58**, e2019RG000660, https://doi.org/10.1029/2019RG000660.

Bjordal, J., T. Storelvmo, K. Alterskjær, and T. Carlsen, 2020: Equilibrium climate sensitivity above 5°C plausible due to state-dependent cloud feedback. *Nat. Geosci.*, **13**, 718–721, https://doi.org/10.1038/s41561-020-00649-1.

Bogenschutz, P. A., A. Gettelman, H. Morrison, V. E. Larson, C. Craig, and D. P. Schanen, 2013: Higher-order turbulence closure and its impact on climate simulations in the Community Atmosphere Model. *J. Climate*, **26**, 9655–9676, https://doi.org/10.1175/JCLI-D-13-00075.1.

Bony, S., M. J. Webb, C. Bretherton, S. A. Klein, P. Siebesma, G. Tselioudis, and M. Zhang, 2011: CFMIP: Towards a better evaluation and understanding of clouds and cloud feedbacks in CMIP5 models. *CLIVAR Exchanges*, No. 56, International CLIVAR Project Office, Southampton, United Kingdom, 20–23.

Boucher, O., and Coauthors, 2013: Clouds and aerosols. *Climate Change 2013: The Physical Science Basis*, T. F. Stocker et al., Eds., Cambridge University Press, 571–657.

Carslaw, K. S., 2022: Aerosol in the climate system. *Aerosols and Climate*, 1st ed. K. S. Carslaw, Ed., Elsevier, 9–52, https://doi.org/10.1016/B978-0-12-819766-0.00008-0.

——, and K. Pringle, 2022: Global aerosol properties. *Aerosols and Climate*, 1st ed. K. S. Carslaw, Ed., Elsevier, 101–133, https://doi.org/10.1016/B978-0-12-819766-0.00011-0.

——, and Coauthors, 2013: Large contribution of natural aerosols to uncertainty in indirect forcing. *Nature*, **503**, 67–71, https://doi.org/10.1038/nature12674.

Ceppi, P., and J. M. Gregory, 2017: Relationship of tropospheric stability to climate sensitivity and Earth's observed radiation budget. *Proc. Natl. Acad. Sci. USA*, **114**, 13 126–13 131, https://doi.org/10.1073/pnas.1714308114.

Cess, R. D., and G. L. Potter, 1988: A methodology for understanding and intercomparing atmospheric climate feedback processes in general circulation models. *J. Geophys. Res.*, **93**, 8305–8314, https://doi.org/10.1029/JD093iD07p08305.

——, and Coauthors, 1990: Intercomparison and interpretation of climate feedback processes in 19 atmospheric general circulation models. *J. Geophys. Res.*, **95**, 16 601–16 615, https://doi.org/10.1029/JD095iD10p16601.

——, and Coauthors, 1996: Cloud feedback in atmospheric general circulation models: An update. *J. Geophys. Res.*, **101**, 12 791–12 794, https://doi.org/10.1029/96JD00822.

Danabasoglu, G., and Coauthors, 2020: The Community Earth System Model Version 2 (CESM2). *J. Adv. Model. Earth Syst.*, **12**, e2019MS001916, https://doi.org/10.1029/2019MS001916.

Deser, C., and Coauthors, 2020: Isolating the evolving contributions of anthropogenic aerosols and greenhouse gases: A new CESM1 large ensemble community resource. *J. Climate*, **33**, 7835–7858, https://doi.org/10.1175/JCLI-D-20-0123.1.

Dong, Y., C. Proistosescu, K. C. Armour, and D. S. Battisti, 2019: Attributing historical and future evolution of radiative feedbacks to regional warming patterns using a Green's function approach: The preeminence of the western Pacific. *J. Climate*, **32**, 5471–5491, https://doi.org/10.1175/JCLI-D-18-0843.1.

Douglas, A., and T. L'Ecuyer, 2019: Quantifying variations in shortwave aerosol–cloud–radiation interactions using local meteorology and cloud state constraints. *Atmos. Chem. Phys.*, **19**, 6251–6268, https://doi.org/10.5194/acp-19-6251-2019.

Emmons, L. K., and Coauthors, 2020: The chemistry mechanism in the Community Earth System Model version 2 (CESM2). *J. Adv. Model. Earth Syst.*, **12**, e2019MS001882, https://doi.org/10.1029/2019MS001882.

Eyring, V., and Coauthors, 2021: Human influence on the climate system. *Climate Change 2021: The Physical Science Basis*, V. Masson-Delmotte et al., Eds., Cambridge University Press, 423–552, https://doi.org/10.1017/9781009157896.005.

Forster, P., and Coauthors, 2021: The Earth's energy budget, climate feedbacks and climate sensitivity. *Climate Change 2021: The Physical Science Basis*, V. Masson-Delmotte et al., Eds., Cambridge University Press, 923–1054, https://doi.org/10.1017/9781009157896.009.

Gettelman, A., and H. Morrison, 2015: Advanced two-moment bulk microphysics for global models. Part I: Off-line tests and comparison with other schemes. *J. Climate*, **28**, 1268–1287, https://doi.org/10.1175/JCLI-D-14-00102.1.

——, ——, and S. J. Ghan, 2008: A new two-moment bulk stratiform cloud microphysics scheme in the Community Atmosphere Model, version 3 (CAM3). Part II: Single-column and global results. *J. Climate*, **21**, 3660–3679, https://doi.org/10.1175/2008JCLI2116.1.

——, ——, S. Santos, P. Bogenschutz, and P. M. Caldwell, 2015: Advanced two-moment bulk microphysics for global models. Part II: Global model solutions and aerosol–cloud interactions. *J. Climate*, **28**, 1288–1307, https://doi.org/10.1175/JCLI-D-14-00103.1.

——, and Coauthors, 2019: High climate sensitivity in the Community Earth System Model Version 2 (CESM2). *Geophys. Res. Lett.*, **46**, 8329–8337, https://doi.org/10.1029/2019GL083978.

Ghan, S. J., 2013: Technical note: Estimating aerosol effects on cloud radiative forcing. *Atmos. Chem. Phys.*, **13**, 9971–9974, https://doi.org/10.5194/acp-13-9971-2013.

Glenn, I. B., G. Feingold, J. J. Gristey, and T. Yamaguchi, 2020: Quantification of the radiative effect of aerosol–cloud interactions in shallow continental cumulus clouds. *J. Atmos. Sci.*, **77**, 2905–2920, https://doi.org/10.1175/JAS-D-19-0269.1.

Grandey, B. S., and C. Wang, 2019: Background conditions influence the estimated cloud radiative effects of anthropogenic aerosol emissions from different source regions. *J. Geophys. Res. Atmos.*, **124**, 2276–2295, https://doi.org/10.1029/2018JD029644.

Hartmann, D. L., and K. Larson, 2002: An important constraint on tropical cloud—Climate feedback. *Geophys. Res. Lett.*, **29**, 1951, https://doi.org/10.1029/2002GL015835.

Heald, C. L., D. J. Jacob, R. J. Park, B. Alexander, T. D. Fairlie, R. M. Yantosca, and D. A. Chu, 2006: Transpacific transport of Asian anthropogenic aerosols and its impact on surface air quality in the United States. *J. Geophys. Res.*, **111**, D14310, https://doi.org/10.1029/2005JD006847.

Hegg, D. A., D. S. Covert, H. H. Jonsson, and R. K. Woods, 2010: The contribution of anthropogenic aerosols to aerosol light-scattering and CCN activity in the California coastal zone. *Atmos. Chem. Phys.*, **10**, 7341–7351, https://doi.org/10.5194/acp-10-7341-2010.

Hoell, J. M., D. D. Davis, S. C. Liu, R. E. Newell, H. Akimoto, R. J. McNeal, and R. J. Bendura, 1997: The Pacific Exploratory Mission-West Phase B: February-March, 1994. *J. Geophys. Res.*, **102**, 28 223–28 239, https://doi.org/10.1029/97JD02581.

Hoesly, R. M., and Coauthors, 2018: Historical (1750–2014) anthropogenic emissions of reactive gases and aerosols from the Community Emissions Data System (CEDS). *Geosci. Model Dev.*, **11**, 369–408, https://doi.org/10.5194/gmd-11-369-2018.

Hoose, C., J. E. Kristjánsson, J.-P. Chen, and A. Hazra, 2010: A classical-theory-based parameterization of heterogeneous ice nucleation by mineral dust, soot, and biological particles in a global climate model. *J. Atmos. Sci.*, **67**, 2483–2503, https://doi.org/10.1175/2010JAS3425.1.

Hurrell, J. W., J. J. Hack, D. Shea, J. M. Caron, and J. Rosinski, 2008: A new sea surface temperature and sea ice boundary dataset for the Community Atmosphere Model. *J. Climate*, **21**, 5145–5153, https://doi.org/10.1175/2008JCLI2292.1.

Huusko, L. L., F. A.-M. Bender, A. M. L. Ekman, and T. Storelvmo, 2021: Climate sensitivity indices and their relation with projected temperature change in CMIP6 models. *Environ. Res. Lett.*, **16**, 064095, https://doi.org/10.1088/1748-9326/ac0748.

Lawrence, D. M., and Coauthors, 2019: The Community Land Model version 5: Description of new features, benchmarking, and impact of forcing uncertainty. *J. Adv. Model. Earth Syst.*, **11**, 4245–4287, https://doi.org/10.1029/2018MS001583.

Liu, X., P.-L. Ma, H. Wang, S. Tilmes, B. Singh, R. C. Easter, S. J. Ghan, and P. J. Rasch, 2016: Description and evaluation of a new four-mode version of the Modal Aerosol Module (MAM4) within version 5.3 of the Community Atmosphere Model. *Geosci. Model Dev.*, **9**, 505–522, https://doi.org/10.5194/gmd-9-505-2016.

Loeb, N. G., S.-H Ham, R. P. Allan, T. J. Thorsen, B. Meyssignac, S. Kato, G. C. Johnson, and J. M. Lyman, 2024: Observational assessment of changes in earth's energy imbalance since 2000. *Surv. Geophys.*, https://doi.org/10.1007/s10712-024-09838-8.

Mechoso, C. R., and Coauthors, 2014: Ocean–cloud–atmosphere–land interactions in the southeastern Pacific: The VOCALS program. *Bull. Amer. Meteor. Soc.*, **95**, 357–375, https://doi.org/10.1175/BAMS-D-11-00246.1.

Meehl, G. A., C. A. Senior, V. Eyring, G. Flato, J.-F. Lamarque, R. J. Stouffer, K. E. Taylor, and M. Schlund, 2020: Context for interpreting equilibrium climate sensitivity and transient climate response from the CMIP6 Earth system models. *Sci. Adv.*, **6**, eaba1981, https://doi.org/10.1126/sciadv.aba1981.

Morrison, H., and A. Gettelman, 2008: A new two-moment bulk stratiform cloud microphysics scheme in the Community Atmosphere Model, version 3 (CAM3). Part I: Description and numerical tests. *J. Climate*, **21**, 3642–3659, https://doi.org/10.1175/2008JCLI2105.1.

Myers, T. A., R. C. Scott, M. D. Zelinka, S. A. Klein, J. R. Norris, and P. M. Caldwell, 2021: Observational constraints on low cloud feedback reduce uncertainty of climate sensitivity. *Nat. Climate Change*, **11**, 501–507, https://doi.org/10.1038/s41558-021-01039-0.

Myhre, G., and Coauthors, 2013: Anthropogenic and natural radiative forcing. *Climate Change 2013: The Physical Science Basis*, T. F. Stocker et al., Eds., Cambridge University Press, 659–740.

Pan, S., and Coauthors, 2020: Larger sensitivity of Arctic precipitation phase to aerosol than greenhouse gas forcing. *Geophys. Res. Lett.*, **47**, e2020GL090452, https://doi.org/10.1029/2020GL090452.

Patnaude, R., and M. Diao, 2020: Aerosol indirect effects on cirrus clouds based on global aircraft observations. *Geophys. Res. Lett.*, **47**, e2019GL086550, https://doi.org/10.1029/2019GL086550.

Persad, G. G., 2023: The dependence of aerosols' global and local precipitation impacts on the emitting region. *Atmos. Chem. Phys.*, **23**, 3435–3452, https://doi.org/10.5194/acp-23-3435-2023.

——, and K. Caldeira, 2018: Divergent global-scale temperature effects from identical aerosols emitted in different regions. *Nat. Commun.*, **9**, 3289, https://doi.org/10.1038/s41467-018-05838-6.

Pincus, R., and M. B. Baker, 1994: Effect of precipitation on the albedo susceptibility of clouds in the marine boundary layer. *Nature*, **372**, 250–252, https://doi.org/10.1038/372250a0.

Qu, X., A. Hall, S. A. Klein, and P. M. Caldwell, 2014: On the spread of changes in marine low cloud cover in climate model simulations of the 21st century. *Climate Dyn.*, **42**, 2603–2626, https://doi.org/10.1007/s00382-013-1945-z.

Raghuraman, S. P., D. Paynter, R. Menzel, and V. Ramaswamy, 2023: Forcing, cloud feedbacks, cloud masking, and internal variability in the cloud radiative effect satellite record. *J. Climate*, **36**, 4151–4167, https://doi.org/10.1175/JCLI-D-22-0555.1.

——, B. Medeiros, and A. Gettelman, 2024: Observational quantification of tropical high cloud changes and feedbacks. *J. Geophys. Res. Atmos.*, **129**, e2023JD039364, https://doi.org/10.1029/2023JD039364.

Rayner, N. A., D. E. Parker, E. B. Horton, C. K. Folland, L. V. Alexander, D. P. Rowell, E. C. Kent, and A. Kaplan, 2003: Global analyses of sea surface temperature, sea ice, and night marine air temperature since the late nineteenth century. *J. Geophys. Res.*, **108**, 4407, https://doi.org/10.1029/2002JD002670.

Rodgers, K. B., and Coauthors, 2021: Ubiquity of human-induced changes in climate variability. *Earth Syst. Dyn.*, **12**, 1393–1411, https://doi.org/10.5194/esd-12-1393-2021.

Rugenstein, M., M. Zelinka, K. B. Karnauskas, P. Ceppi, and T. Andrews, 2023: Patterns of surface warming matter for climate sensitivity. *Eos*, **104**, https://doi.org/10.1029/2023EO230411.

Seager, R., N. Henderson, and M. Cane, 2022: Persistent discrepancies between observed and modeled trends in the tropical Pacific Ocean. *J. Climate*, **35**, 4571–4584, https://doi.org/10.1175/JCLI-D-21-0648.1.

Sherwood, S. C., S. Bony, and J.-L. Dufresne, 2014: Spread in model climate sensitivity traced to atmospheric convective mixing. *Nature*, **505**, 37–42, https://doi.org/10.1038/nature12829.

——, and Coauthors, 2020: An assessment of Earth's climate sensitivity using multiple lines of evidence. *Rev. Geophys.*, **58**, e2019RG000678, https://doi.org/10.1029/2019RG000678.

Shi, X., X. Liu, and K. Zhang, 2015: Effects of pre-existing ice crystals on cirrus clouds and comparison between different ice nucleation parameterizations with the Community Atmosphere Model (CAM5). *Atmos. Chem. Phys.*, **15**, 1503–1520, https://doi.org/10.5194/acp-15-1503-2015.

Shindell, D., and G. Faluvegi, 2009: Climate response to regional radiative forcing during the twentieth century. *Nat. Geosci.*, **2**, 294–300, https://doi.org/10.1038/ngeo473.

Simpson, I. R., and Coauthors, 2023: The CESM2 single-forcing large ensemble and comparison to CESM1: Implications for experimental design. *J. Climate*, **36**, 5687–5711, https://doi.org/10.1175/JCLI-D-22-0666.1.

Smith, C. J., and Coauthors, 2020: Effective radiative forcing and adjustments in CMIP6 models. *Atmos. Chem. Phys.*, **20**, 9591–9618, https://doi.org/10.5194/acp-20-9591-2020.

Smith, D. M., and Coauthors, 2022: Attribution of multi-annual to decadal changes in the climate system: The Large Ensemble Single Forcing Model Intercomparison Project (LESFMIP). *Front. Climate*, **4**, 955414, https://doi.org/10.3389/fclim.2022.955414.

Soden, B. J., A. J. Broccoli, and R. S. Hemler, 2004: On the use of cloud forcing to estimate cloud feedback. *J. Climate*, **17**, 3661–3665, https://doi.org/10.1175/1520-0442(2004)017<3661:OTUOCF>2.0.CO;2.

Storelvmo, T., 2017: Aerosol effects on climate via mixed-phase and ice clouds. *Annu. Rev. Earth Planet. Sci.*, **45**, 199–222, https://doi.org/10.1146/annurev-earth-060115-012240.

Szopa, S., and Coauthors, 2021: Short-lived climate forcers. *Climate Change 2021: The Physical Science Basis*, V. Masson-Delmotte et al., Eds., Cambridge University Press, 817–922, https://doi.org/10.1017/9781009157896.008.

Tan, I., T. Storelvmo, and M. D. Zelinka, 2016: Observational constraints on mixed-phase clouds imply higher climate sensitivity. *Science*, **352**, 224–227, https://doi.org/10.1126/science.aad5300.

Taylor, K. E., D. Williamson, and F. Zwiers, 2000: The sea surface temperature and sea-ice concentration boundary conditions for AMIP II simulations, PCMDI Rep. 60, 28 pp.

Twomey, S., 1974: Pollution and the planetary albedo. *Atmos. Environ.*, **8**, 1251–1256, https://doi.org/10.1016/0004-6981(74)90004-3.

——, 1977: The influence of pollution on the shortwave albedo of clouds. *J. Atmos. Sci.*, **34**, 1149–1152, https://doi.org/10.1175/1520-0469(1977)034<1149:TIOPOT>2.0.CO;2.

Wang, C., B. J. Soden, W. Yang, and G. A. Vecchi, 2021: Compensation between cloud feedback and aerosol-cloud interaction in CMIP6 models. *Geophys. Res. Lett.*, **48**, e2020GL091024, https://doi.org/10.1029/2020GL091024.

Wang, Y., X. Liu, C. Hoose, and B. Wang, 2014: Different contact angle distributions for heterogeneous ice nucleation in the Community Atmospheric Model version 5. *Atmos. Chem. Phys.*, **14**, 10 411–10 430, https://doi.org/10.5194/acp-14-10411-2014.

Webb, M. J., and Coauthors, 2017: The Cloud Feedback Model Intercomparison Project (CFMIP) contribution to CMIP6. *Geosci. Model Dev.*, **10**, 359–384, https://doi.org/10.5194/gmd-10-359-2017.

Wilcox, L. J., E. J. Highwood, B. B. B. Booth, and K. S. Carslaw, 2015: Quantifying sources of inter-model diversity in the cloud albedo effect. *Geophys. Res. Lett.*, **42**, 1568–1575, https://doi.org/10.1002/2015GL063301.

Wills, R. C. J., Y. Dong, C. Proistosecu, K. C. Armour, and D. S. Battisti, 2022: Systematic climate model biases in the large-scale patterns of recent sea-surface temperature and sea-level pressure change. *Geophys. Res. Lett.*, **49**, e2022GL100011, https://doi.org/10.1029/2022GL100011.

Zelinka, M. D., and D. L. Hartmann, 2010: Why is longwave cloud feedback positive? *J. Geophys. Res.*, **115**, D16117, https://doi.org/10.1029/2010JD013817.

——, D. A. Randall, M. J. Webb, and S. A. Klein, 2017: Clearing clouds of uncertainty. *Nat. Climate Change*, **7**, 674–678, https://doi.org/10.1038/nclimate3402.

——, T. A. Myers, D. T. McCoy, S. Po-Chedley, P. M. Caldwell, P. Ceppi, S. A. Klein, and K. E. Taylor, 2020: Causes of higher climate sensitivity in CMIP6 models. *Geophys. Res. Lett.*, **47**, e2019GL085782, https://doi.org/10.1029/2019GL085782.

Zhao, A., D. S. Stevenson, and M. A. Bollasina, 2019: Climate forcing and response to greenhouse gases, aerosols, and ozone in CESM1. *J. Geophys. Res. Atmos.*, **124**, 13 876–13 894, https://doi.org/10.1029/2019JD030769.

Zhou, C., M. D. Zelinka, and S. A. Klein, 2017: Analyzing the dependence of global cloud feedback on the spatial pattern of sea surface temperature change with a Green's function approach. *J. Adv. Model. Earth Syst.*, **9**, 2174–2189, https://doi.org/10.1002/2017MS001096.